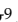
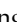
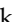


Research Paper

Versatile and Finely Tuned Albumin Nanoplatfom based on Click Chemistry

Ji Yong Park^{1,5*}, Myung Geun Song^{1,8*}, Kyu Wan Kim¹, Nadeem Ahmed Lodhi^{1,7}, Jin Yeong Choi², Young Ju Kim^{1,3,4}, Jung Young Kim⁶, Hyewon Chung⁹, Chiwoo Oh², Yun-Sang Lee^{1,3}, Keon Wook Kang^{1,3,4}, Hyung-Jun Im², Seung Hyeok Seok⁹, Dong Soo Lee^{1,2}, Edmund E. Kim¹, Jae Min Jeong^{1,3,4}

1. Department of Nuclear Medicine, Seoul National University Hospital, College of Medicine, Seoul, South Korea.
2. Graduate School of Convergence Science and Technology, Seoul National University, Seoul, South Korea.
3. Radiation Medicine Research Institute, Seoul National University College of Medicine, Seoul, South Korea.
4. Cancer Research Institute, Seoul National University, Seoul, South Korea.
5. Department of Biomedical Sciences, Seoul National University, Seoul, South Korea.
6. Department of RI Technology-Convergence, Korean Institute of Radiological & Medical Sciences (KIRAMS), Seoul, South Korea.
7. Isotope Production Division, Pakistan Institute of Nuclear Science & Technology (PINSTECH), P. O, Nilore, Islamabad.
8. Biomedical Research Institute, Seoul National University Hospital, Seoul, South Korea.
9. Department of Microbiology and Immunology, Institute of Endemic Disease, College of Medicine, Seoul National University, Seoul, South Korea.

* These authors contributed equally.

✉ Corresponding authors: Yun-Sang Lee, PhD. Email: wonza43@snu.ac.kr Address: 101 Daehak-ro, Jongno-gu, Seoul, Republic of Korea (zip: 03080). Keon Wook Kang, MD, PhD. Email: kangkw@snu.ac.kr Address: 101 Daehak-ro, Jongno-gu, Seoul, Republic of Korea (zip: 03080). Hyung-Jun Im, MD, PhD. Email: iihjj@gmail.com Address: 18-dong, Gwanak-ro 1, Gwanak-gu, Seoul, Republic of Korea, (zip: 08826).

© Ivyspring International Publisher. This is an open access article distributed under the terms of the Creative Commons Attribution (CC BY-NC) license (<https://creativecommons.org/licenses/by-nc/4.0/>). See <http://ivyspring.com/terms> for full terms and conditions.

Received: 2019.01.14; Accepted: 2019.04.30; Published: 2019.05.18

Abstract

Albumin is one of the most attractive nanoplatfoms for targeted imaging and drug delivery due to its biocompatibility and long circulation half-life. However, previously reported albumin-based nanoplatfoms have shown inconsistent blood circulation half-life according to the modified methods, and the affecting factors were not well evaluated, which could hamper the clinical translation of albumin-based nanoplatfoms. Herein, we developed a finely tuned click-chemistry based albumin nanoplatfom (CAN) with a longer circulation half-life and an efficient tumor targeting ability.

Methods: CAN was synthesized in two steps. First, albumin was conjugated with ADIBO-NHS (albumin-ADIBO) by reacting albumin with various molar ratios of ADIBO. The number of attached ADIBO moieties was determined using matrix-assisted laser desorption ionization time of flight (MALDI-TOF). Second, the desired modalities including azide-functionalized chelator, a fluorescence dye, and folate were incorporated into albumin-ADIBO using strain-promoted alkyne-azide cycloaddition reaction (SPAAC reaction). The biodistribution and targeting efficiency of functionalized CANs were demonstrated in mice.

Results: The degree of functionalization (DOF) and resulting *in vivo* biodistribution was controlled precisely using the click chemistry approach. Specifically, the numbers of attached azadibenzocyclooctyne (ADIBO) moieties on albumin, the DOF, were optimized by reacting albumin with varying molar ratios of ADIBO with a high reproducibility. Furthermore, we developed a simple and efficient method to estimate the DOF using *UV-visible* spectrophotometry (UV-vis), which was further validated by matrix-assisted laser desorption ionization time of flight (MALDI-TOF). The biodistribution of CAN could be controlled by DOF, and CAN with an optimized DOF showed a long circulation half-life (> 18 h). CAN was further functionalized using a simple click chemistry reaction with an azide functionalized chelator, a fluorescence dye, and folate. ⁶⁴Cu- and folate-labeled CAN (⁶⁴Cu-CAN-FA) showed effective and specific folate receptor targeting *in vivo*, with an over two-fold higher uptake than the liver at 24 h post-injection.

Conclusions: Our development from the precisely controlled DOF demonstrates that an optimized CAN can be used as a multifunctional nanoplatfom to obtain a longer half-life with radioisotopes and ligands, and provides an effective method for the development of albumin-based tumor theranostic agents.

Key words: albumin, click chemistry, positron emission tomography, theranostics

Introduction

Albumin is the most abundant protein in plasma and consists of a single chain amino acid weighing 66.7 kDa [1]. Albumin has been extensively explored as a drug delivery carrier and nanoplatform because of the possibility to carry out modifications, as well as its long circulation half-life, small size, and excellent biocompatibility [2, 3]. In particular, the long circulation half-life of albumin (serum half-life of 19-22 days) is an important feature that allows to maintain a high drug concentration in the blood for a longer period of time and enhances the efficiency of delivery to the target site [4]. Various methodologies have been exploited to utilize the properties of albumin for the delivery of the drugs. Human serum albumin (HSA) has two intrinsic binding sites: a warfarin binding site (site I) and a benzodiazepine binding site (site II) [5]. The chemotherapeutic, anti-inflammatory, and hypoglycemic drugs bind to the intrinsic binding sites by non-covalent van der Waals forces electrostatic interactions or hydrophobic interactions [3, 6, 7]. The classic examples of non-covalent interactions are radioactive ^{111}In - and $^{99\text{m}}\text{Tc}$ -labeled macro-aggregated albumin (^{111}In -MAA and $^{99\text{m}}\text{Tc}$ -MAA), which are widely used for gastrointestinal bleeding and lung perfusion by single photon emission computed tomography (SPECT) [8, 9]. Albumin can also serve as a template or scaffold to enhance the distribution and pharmacokinetic profile of the drug to the tumor by the nanoparticles [10-12]. However, the circulation half-life of various albumin nanoplatforms was much shorter than that of albumin in most studies and was inconsistent according to the modification methods. For example, $^{99\text{m}}\text{Tc}$ -labeled HSA has a very short circulation half-life (32 minutes), and has been applied clinically for several decades [13-15]. Other albumin nanoplatforms with a longer circulation half-life (4.8 h) have been reported [16, 17]. However, it has yet to be evaluated which factor is affecting or how to control the distribution of the albumin nanoplatforms.

Recently, the covalent attachment of the drug molecules to the amino or carboxylic groups in albumin has also been used for the functionalization of albumin for specific targeting and *in vivo* imaging [18, 19]. However, in the covalent conjugation-based method, controlling the binding of functional groups on albumin is very difficult. Importantly, the actual binding ratio of albumin and the functional groups or drugs are difficult to predict and evaluate. The unpredicted binding ratio of the functional groups to albumin inevitably raises concerns about an uncontrolled surface chemistry and unfavorable distribution profiles [20].

To circumvent the problem, click chemistry was used to overcome the limitation of uncontrolled conjugation. Click chemistry refers to a collection of reactions that have fast reaction rate and excellent orthogonality which has been utilized for the development of targeted nanoplatform [21]. Click chemistry can be performed in a biocompatible aqueous condition, which is a huge advantage for the preservation of soft nanomaterials including albumin during the functionalization [22]. Furthermore, click chemistry has good orthogonality which is beneficial for precise control of the degree of functionalization (DOF) [23].

Herein, we developed a click chemistry-based albumin nanoplatform (CAN) with attention to achieving a long circulation half-life. We use ^{64}Cu -labeled CAN (^{64}Cu -CAN) with different DOF to study the distribution profile of click-based CAN in normal mice. The metallic isotope ^{64}Cu ($t_{1/2} = 12.7$ h, $\beta^+ = 655$ keV (17.8%), $\beta^- = 579$ keV (38.4%)) with longer half-life is selected for PET imaging and targeted radiotherapy [24] [25], allowing the pharmacokinetic and distribution of CAN to be evaluated by performing series of PET images in the same animal for several hours. To further explore the properties of CAN, ^{64}Cu -labeled CAN folate conjugates were synthesized and tested for their efficacy to target the folate receptors, which were overexpressed in wide varieties of cancer, including breast, lung, and ovarian cancers [26, 27]. To the best of our knowledge, albumin nanoplatform, which has the controllable DOF and specific targeting ability, has not been reported.

Materials and Methods

All chemicals were of reagent grade and used without further purification. 2,5-dioxopyrrolidin-1-yl-4-azidobutanoate (N_3 -NHS), azadibenzocyclooctyne-NHS ester (ADIBO-NHS), 2,2',2''-(2-(4-(3-(3-azidopropyl)thioureido)benzyl)-1,4,7-triazonane-1,4,7-triyl)triacetic acid (N_3 -NOTA), and Flamma 648 azide (N_3 -FNR648) were purchased from FutureChem Co., Ltd (Seoul, Korea). N_2 -(4-(4-(((2-amino-4-oxo-3,4-dihydropteridin-6-yl)methyl)amino)benzamido)-4-carboxybutanoyl)glycylglycyl-L-cysteinyl-L-glutamyl-N-6-(4-azidobutanoyl)-L-lysine (N_3 -folate) was purchased from PEPTRON (Daejeon, Korea). All other reagents and chemicals were purchased from Sigma-Aldrich (St. Louis, MO, USA) and used without further purification. Instant thin layer chromatography-silica gel (ITLC-SG) was purchased from Agilent Technologies, Inc. (Santa Clara, CA, USA). PD-10 desalting column was obtained from GE Healthcare (Buckinghamshire, UK). Radioactivity was measured using a gamma scintillation counter

(Packard Cobra II, GMI, NM, USA). The molecular weights of albumin and its conjugates were determined by matrix-assisted laser desorption ionization time of flight/time of flight mass spectrometry (MALDI-TOF/TOF MS) using the TOF/TOF 5800 system (AB Sciex, Foster City, CA, USA). The hydrodynamic diameter and size distribution of nanoplateforms were analyzed using a dynamic light scattering (DLS) system Zetasizer Nano ZS90 (Malvern Instruments Ltd, Worcestershire, UK). The concentration of albumin was measured by ultraviolet-visible spectrometry (UV-vis) using NanoDrop® ND-1000 (NanoDrop Technologies, Wilmington, DE, USA).

Albumin conjugation with ADIBO-NHS

Human Albumin Fraction V was purchased from MP Biomedicals (Aurora, Ohio, USA). Albumin was dissolved in phosphate buffered saline (PBS) at a concentration of 1 mg/mL, and the solution was aliquoted to 0.5 mg/0.5 mL per reaction vial. ADIBO-NHS were dissolved in DMSO (5 mg/125 µL) and added to PBS to reach a volume of 500 µL. NHS-compounds were added to a reaction vial by varying the molar ratio (NHS-compounds:albumin, 1.1:1, 3.4:1, 5.7:1, 8.1:1, 11.4:1, 17.2:1, and 23:1; the seven conjugates were named Rxn R1, Rxn R3, Rxn R6, Rxn R8, Rxn R11, Rxn R17, and Rxn R23, respectively). The reaction vials were incubated at room temperature for 2 h and size exclusion chromatography (PD-10 column) was performed using PBS as the mobile phase. A droplet of each fraction was spotted on a glass microfiber filter (Whatman GF/B) before staining with Coomassie blue solution. Fractions showing blue stained droplets were collected for albumin concentration analysis. UV-Vis spectroscopy was used to quantify albumin concentration (µg/µL) by determining the optical density ratio at 260/280 nm. The albumin-ADIBO conjugate was lyophilized for further experiments.

Preparation of folic acid (FA) and fluorescence (FI) conjugated albumin

To obtain CAN-FI, N₃-FNR648 (120 nmol/12 µL, dissolved in DMSO) was added to Rxn R6 (60 nmol/1 mL, dissolved in PBS) and incubated at 4°C for 30 min. This conjugate was further purified using the PD-10 desalting column eluted with PBS. For albumin conjugates with targeting moiety, targeting compound of N₃-folate (**Figure S1A**) was reacted with CAN-FI using a 2-fold molar excess prior to radio-labeling, which was denoted as CAN-FA-FI (CAN-FI was conjugated with N₃-folate).

Radiolabeling of N₃-NOTA

The vial containing radioisotopes (⁶⁴Cu, ⁶⁸Ga,

¹⁷⁷Lu) was dried using a stream of dry nitrogen. After the vial was completely dried, the pH was adjusted to 5 with 1 M sodium acetate buffer (pH 5.3, 100 µL). N₃-NOTA (15 nmole, volume) was added and heated at 60°C for 30 min on the heating block. Radiolabeling efficiency and stability were determined using radio-instant thin layer chromatography-silica gel (radio-ITLC-SG) using 0.1 M citric acid as the mobile phase (R_f of radiolabeled N₃-NOTA = 0.4–0.5; R_f of free radioisotope = 0.9–1.0; R_f of radiolabeled albumin conjugate = 0.0–0.1). Radiolabeling stability was evaluated at 0, 4, 24, and 48 h.

Determination of the conjugation number of ADIBO-NHS

MALDI-TOF/TOF MS was performed to determine the number of ADIBO-NHS moieties conjugated to albumin (degree of functionalization = DOF). An aliquot of albumin solution (10 µL) was mixed with a saturated solution of α-cyano-4-hydroxy-cinnamic acid in a mixture of acetonitrile and water containing 0.1% TFA (1:1 v/v), and each sample (1 µL) was spotted on MALDI plates and allowed to dry completely at room temperature. Measurements were acquired in the linear mode with an accelerating voltage of 25 kV. The analytes were ablated with a 337 nm nitrogen laser. The analysis was performed with 125 scans with 20 laser shots per scan. The molecular weights of albumin and albumin-ADIBO were calculated as the average of the results from 2500 laser shots. The conjugation number of the ADIBO group on albumin and DOF were also predicted by analyzing the absorbance of albumin-ADIBO by UV-vis.

Analysis of zeta potential and size of albumin conjugates

The hydrodynamic diameter and zeta potential of the CAN were analyzed using a DLS system. The hydrodynamic size distribution was measured using a homogeneously diluted albumin solution (10-fold, the molar range of 1–10 µM) using PBS. The zeta potentials were also measured from a 100-fold diluted Alb solution using PBS (molar range, 0.1–1 µM) in a zeta potential cuvette.

Analysis of morphology of albumin conjugates by transmission electron microscopy

The morphology of albumin CAN with DOF5, and ⁶⁴Cu-CAN-FA was analyzed using a transmission electron microscope (TEM, JEM-1400, JEOL, USA). One droplet of sample (10 µL) was spotted on the 200-mesh copper grid coated with carbon and absorbed onto filter paper. The grid was dried for 30 min on a grid container and examined by TEM.

Flow cytometry

KB and PC3 cells were obtained from the Korea Cell Line Bank (Seoul, Korea). PC3 cells were cultured in RPMI 1640 medium supplemented with 10% fetal bovine serum (BSA) and 1% Anti-Anti (Gibco by Life Technologies, CA, USA) in a 5% CO₂ humidified incubator at 37°C. KB cells were cultured under the same conditions, except for the use of folate-deficient RPMI. Flow cytometry was performed to assess the folate receptor expression of the cell lines. We used purified anti-human folate receptors α and β (FR- $\alpha\beta$) antibody (BioLegend, CA, USA, Cat. 391802) and Alexa Fluor® 647 anti-rat IgG2a Antibody (Biolegend, CA, USA, Cat. 407511) as the secondary antibodies. For the flow cytometry using CAN, 1×10^6 cells/mL cells were suspended in cold (PBS) containing 0.5% BSA and CAN-FA-FI or CAN-FI (200 $\mu\text{g}/\text{mL}$) was added to PBS/0.5% BSA before incubating for 30 min. Then, the incubation media was aspirated and the cells were washed three times with cold PBS. After re-suspending in cold PBS at a concentration of 250 cells/ μL , the cells were analyzed using the Millipore Guava easyCyte and InCyte software.

In vitro fluorescence imaging

KB cells were seeded on 8-well culture slides in an 8-well Lab-Tek Chamber Slide system (ThermoFisher Scientific Inc., USA). Twenty-four hours after seeding, the cells were washed with sterile HBSS containing 1% (v/v) BSA (HBSS/BSA). To examine the *in vitro* specific cellular uptake, 3 nmol Alb conjugates in 1200 μL HBSS/HBA with targeting moiety (FA-CAN-FI) was added to the culture medium in each well containing KB cells. An excess molar amount (300 nmol) of folate peptide was added to the culture medium for blocking and was incubated equally as that of control. To assess the non-specific albumin uptake of the cells, identical procedures were carried out using albumin conjugate without folate moiety. Samples were incubated in a 5% CO₂ humidified incubator at 37°C, washed with HBSS/BSA three times before confocal laser microscopic imaging. 4', 6-diamidino-2-phenylindole (DAPI) was used for nuclear staining. Cell fluorescence imaging was performed using a confocal laser scanning microscope (Leica SP8, Leica, Germany) with a 648 nm laser excitation and the fluorescence was collected at wavelengths of 671 nm.

In vivo imaging

All animal experiments were performed in accordance with Institutional Animal Care and Use Committee, Seoul National University Hospital. Six-week-old female nude mice (BALB/c nu/nu) were purchased from Orient Bio (Seongnam, Korea).

Mice were fed a folate-free diet (A08112101, Research Diets, New Brunswick, NJ, USA) for 2–3 weeks to reduce the serum folate level to a physiologic range. KB tumor xenografts were established by subcutaneously inoculating 2×10^6 KB cells suspended in PBS (100 μL) into the lower or upper flank of each mouse. The biodistribution and images were obtained once the tumor had reached an optimal size (100–300 cm³). Positron emission tomography (PET) imaging was carried out on PET scanner G4 (Sofie Biosciences, USA) or PET/CT scanner eXplore VISTA (GE Healthcare, WI, USA) after injecting ⁶⁴Cu-CAN or ⁶⁸Ga-CAN into mice via the tail vein under isoflurane anesthesia. Single-photon emission computed tomography/computed tomography (SPECT/CT) imaging was performed using a four-headed multi-pinhole NanoSPECT (Bioscan Inc., Washington D.C.) after the tail vein injection of ¹⁷⁷Lu-CAN. PET images were analyzed using MIMvista (MIM Software Inc., USA). The three-dimensional region of interest was used for the quantitative evaluation of the uptake in the blood pool, liver, muscle, and tumor (for tumor models). For the estimation of the circulation half-life of the CAN, the time activity curves of blood pool were used and the two-phase decay model was adopted to determine the short distribution half-life ($t_{1/2\alpha}$) and the long elimination half-life ($t_{1/2\beta}$). The long elimination half-life ($t_{1/2\beta}$) was considered as the circulation half-life of the CAN [32].

Blood test for kidney and liver function

Forty-eight hours after the injection of saline, ⁶⁴Cu-CAN, or ⁶⁴Cu-CAN-FA into normal mice, the mice were euthanized and the blood was collected into a BD Vacutainer® K2 EDTA hematology tube (BD Biosciences, Franklin Lakes, NJ, USA) for hematology analysis and BD Vacutainer® SSTTM (BD Biosciences, Franklin Lakes, NJ, USA) for kidney and liver function analysis. The blood collected into the BD Vacutainer® SSTTM was centrifuged at 3000 rpm for 5 min at 4°C and the samples were analyzed to determine the blood creatinine (Cr) levels, blood urea nitrogen (BUN) levels, and aspartate transaminase (AST) and alanine transaminase (ALT) tests.

Hematoxylin and eosin staining of main organs and tumor sections

The images of the hematoxylin and eosin (H&E) stained sections of the main organs and the tumors dissected from the mice treated with ⁶⁴Cu-CAN, ⁶⁴Cu-CAN-FA, ⁶⁴Cu-CAN-FA with Methotrexate, and ⁶⁴Cu-CAN-FA with folate at the experimental endpoint (48 h) were analyzed. The organs and tumors were fixed 48 h with 4% paraformaldehyde for

histopathological examination to assess the safety of radio-labeled CAN *in vivo*.

Blood compatibility test

Five-week-old female mice were euthanized and the blood was collected into BD Vacutainer® K2 EDTA hematology tube (BD Biosciences, Franklin Lakes, NJ, USA) before washing 3 times at 3000 rpm for 5 min with saline. The samples (1 mL) of fresh blood were diluted with 9 mL of saline for hemolysis tests. Then, 50 µL of diluted blood was added to PCR tubes containing 100 µL of saline and 50 µL of the prepared sample. The albumin concentration of the prepared sample was 10 mg/mL, which was prepared in the same manner regardless of the DOF. Saline was used as a negative control (NC), and 0.2% Triton X-100 was used as a positive control (PC). The mixture was incubated at 37 °C for 10 min and centrifuged at 10000 rpm for 5 min. Finally, the supernatant was removed and transferred to 96-well plates to determine the optical density at 350 nm.

$$\text{hemolytic potential (\%)} = 100 \times (\text{treatment group-NC}) / (\text{PC-NC})$$

Cell viability assay

To validate the toxicity of the DOFs, 22RV1, MDA-MB-231, and 293FT cells were seeded in the 96-well plates at a density of 2×10^3 cells/well. They were incubated with DOFs (0, 12.5, 25, 50, 100, and 200 µg/200 µL) for 48 h. The medium was replaced with fresh medium containing CCK-8 reagent (Dojindo, Japan) and the cells were incubated for an additional 2 h at 37 °C. The number of viable cells was assessed by measuring absorbance at 450 nm.

Statistical analysis

Quantitative data were displayed as the mean \pm standard deviation (SD). The agreement of the multiple measurements was assessed using intraclass correlation coefficient (ICC). The means were compared using the one-way ANOVA or Student's *t*-test. *P*-values < 0.05 were considered statistically significant.

Results and Discussion

Preparation and characterization of CAN

Albumin has a large number of carboxyl and amine groups, which can be used to carry out covalent modifications. We used the amine functional group of albumin to carry out the modifications with ADIBO-NHS. The synthesis of albumin conjugates was performed in two steps (Figure 1A). First, albumin was conjugated with ADIBO-NHS

(albumin-ADIBO). Second, the desired imaging modality was incorporated into the albumin-ADIBO conjugate through the strain-promoted alkyne-azide cycloaddition reaction (SPAAC). For example, to label albumin with ^{64}Cu , ^{177}Lu , or ^{68}Ga , a bifunctional chelator containing the terminal azide group '2,2',2''-(2-(4-(3-(3-azidopropyl)thioureido)benzyl)-1,4,7-triazonane-1,4,7-triyl)triacetic acid ($\text{N}_3\text{-NOTA}$) was conjugated with the albumin-ADIBO moiety through the SPAAC reaction ($^{64}\text{Cu-CAN}$, $^{177}\text{Lu-CAN}$, or $^{68}\text{Ga-CAN}$). For *in vitro* fluorescence imaging, albumin-ADIBO was conjugated with an azide-functionalized fluorescence dye (Fl), $\text{N}_3\text{-FNR648}$ (CAN-Fl). For folate (FA) receptor targeting, $\text{N}_3\text{-folate}$ was conjugated to albumin-ADIBO (CAN-FA). For imaging and folate receptor targeting, $\text{N}_3\text{-folate}$ and $\text{N}_3\text{-FNR648}$ were conjugated to albumin-ADIBO (CAN-FA-Fl) (Figure S1B, C). We developed a simple method to control the number of clickable ADIBO (DOF) on albumin. We found that the reaction molar ratio between albumin and ADIBO determines the number of ADIBO attached on albumin reproducibly. According to the reaction molar ratios (ADIBO-NHS : albumin = 1.1 : 1, 3.4 : 1, 5.7 : 1, 8.1 : 1, 11.4 : 1, 17.2 : 1, and 23 : 1), the mass of albumin-ADIBO was increased, indicating that the DOF was increased (Figure 1B). Based on the MALDI-TOF result, we were able to calculate the amount of ADIBO on one albumin and determine the DOF (Figure 1C). We also investigated the albumin and albumin-ADIBO samples using UV-vis. The absorbance peaks were found at 280 nm in albumin, and at 280 and 309 nm in albumin-ADIBO. We also found that the peak intensities of albumin-ADIBO changed according to reaction ratio (Figure 1D, E). Although the absolute amount of albumin was the same in the samples with different reaction ratios, both the absorbance peak intensities at 280 nm (A_{280}) and 309 nm (A_{309}) increased. We tested three batches for each reaction ratio and found that the absorbance peak intensity measurements were highly reproducible with ICC of 0.997 (95% CI: 0.989–0.999) for A_{280} and 0.999 (95% CI: 0.997–0.999) for A_{309} (Table S1A). We considered that the increased peak intensity at 280 nm was caused by an increased peak intensity at 309 nm, thereby confirming the almost perfectly linear relationship ($R^2 = 0.9992$) between the peak intensities. Furthermore, the slope can be used for the correction factor (CF) to estimate the peak intensity caused by albumin (corrected $A_{280} = A_{280c}$) in new albumin-ADIBO samples (Supporting Information (SI), Equation 1). The molar concentration of albumin and ADIBO from albumin-ADIBO could be calculated using A_{280c} , A_{309} , and the specific epsilons of albumin and ADIBO

based on the Beer–Lambert Law (SI, Equation 2) [33]. Finally, the DOF could be estimated by simply dividing the molar concentration of ADIBO by that of albumin (SI, Equation 3). We obtained the A_{280c} and A_{309} of new albumin-ADIBO samples with different reaction molar ratios and calculated the DOF. The calculated DOFs correlated well with the MALDI-TOF results in the same samples with an ICC of 0.991 (95% CI: 0.953–0.998) (Table S1B). This indicates that the DOF of CAN can be estimated quickly and easily using only UV-vis analysis, without performing MALDI-TOF. We prepared click chemistry-based albumin nanoplateforms (CANs) with four different DOFs for further experiments. The CANs with 1, 5, 8, and 13 DOF were denoted as CAN-DOF1, CAN-DOF5, CAN-DOF8, and CAN-DOF13, respectively. The hydrodynamic diameters of the CANs were similar regardless of the DOF (CAN-DOF1 = 8.7 ± 1.2 nm, CAN-DOF5 = 8.8 ± 1.4 nm, CAN-DOF8 = 8.6 ± 1.3 nm, and CAN-DOF13 = 8.6 ± 1.3 nm). However, the zeta-potentials of the CANs decreased when the DOF increased (CAN-DOF1 = -6.84 ± 1.80 mV, CAN-DOF5 = -10.23 ± 2.57 mV, CAN-DOF8 = -14.78 ± 2.91 mV, and CAN-DOF13 = -18.81 ± 3.24 mV) (Figure S2). The morphology of the albumin-based nanoplateforms was examined using transmission electron microscopy (TEM). As revealed by the TEM images, albumin, ADIBO-modified albumin, and ^{64}Cu -CAN-FA showed a uniform morphology with an average size of ~ 20 nm (Figure S3). It is worth mentioning that, unlike conventional albumin nanoclusters with size of 100 nm, CAN maintained the original size and morphology even after various modifications, including conjugation with ADIBO-NHS, click-chemistry reactions to conjugate folic acid, and NOTA-chelated ^{64}Cu .

Radiolabeling of CAN using click chemistry with various radioisotopes

CANs were radiolabeled with ^{64}Cu , ^{68}Ga , and ^{177}Lu in over 98% radiochemical yields determined by radio-ITLC SG (Figure 1F–H). The click reaction of radioisotope-labeled N_3 -NOTA with CAN was conducted under physiological conditions. The click reaction conjugation efficiency after 1 h of incubation by using DOF1, 5, 8, and 13 was over 95% for the all the different types of CAN. The radiochemical stabilities of the ^{64}Cu -CANs were over 95% until 48 h after radiolabeling (Figure S4). In a recent paper, the biodistribution of the alkylphosphocholine analog (NM600) was altered by different radiometal labeling. In the study, the circulation half-lives of ^{86}Y -NM600, ^{64}Cu -NM600, and ^{89}Zr -NM600 were significantly different [34]. Thus, we compared the biodistribution of ^{64}Cu -CAN-DOF5 and

^{177}Lu -CAN-DOF5 and found that the biodistribution was similar between the two CANs (Figure S5).

DOF optimization of CAN for a favorable biodistribution

We hypothesized that the distribution of the CAN could be controlled according to the DOF. For this purpose, we carried out the biodistribution of the ^{64}Cu -labeled CANs with four different DOFs. The serial PET images were obtained at 0, 4, 24, and 48 h after intravenous injection of ^{64}Cu -labeled CANs in the normal nude mice. We found that the biodistribution of the CANs was slightly different according to DOFs (Figure 2A, B, Table S2). The circulation half-life ($t_{1/2\beta}$) of the CANs decreased with increasing DOF (CAN-DOF1 = 20.64 h, CAN-DOF5 = 18.28 h, CAN-DOF8 = 16.42 h, and CAN-DOF13 = 16.10 h) (Table S3). The blood pool activity of CAN-DOF13 was significantly lower than those of the other CANs at 24 h post-injection ($P < 0.01$). In addition, the blood pool uptake of CAN-DOF8 was significantly lower than that of CAN-DOF1 ($P < 0.01$). Meanwhile, the liver uptake of the CAN was increased with increase in DOFs. At 24 h after injection, the liver uptake of CAN-DOF1 was significantly lower than those of CAN-DOF8 ($P < 0.01$) and CAN-DOF13 ($P < 0.01$). The liver uptake of CAN-DOF5 was also significantly lower than those of CAN-DOF8 ($P < 0.01$) and CAN-DOF13 ($P < 0.01$) (Figure 2C). In summary, with an increased DOF, the blood pool uptakes and circulation half-lives of CANs were decreased while the liver uptake was increased. However, there was no significant difference in the biodistribution between CAN-DOF1 and CAN-DOF5. Therefore, we used CAN-DOF5 for further experiments because CAN-DOF1 is limited for multiple functionalizations. In the latter part of the paper, CAN is used to denote CAN-DOF5 unless otherwise stated. The size, shape, charge, surface chemistry, and degree of functionalization of the nanoparticles (NPs) can alter their biodistribution [35–37]. However, the affecting factors have not been well evaluated in albumin nanoplateforms. Furthermore, it has not been reported whether the DOF by click chemistry can alter the biodistribution of NPs. Our finding that DOF can alter the biodistribution even with the same size will be beneficial for the development of theranostic NPs using click chemistry. We found that the surface charge of the CAN varies according to the DOF. However, the different surface charges of CANs may not be the reason for the changes in biodistribution, because it has been reported that different surface charges of albumin nanoparticles do not exhibit different biodistributions [38]. These findings suggest

that the alteration degree of original albumin may promote the recognition of the nanoplatform by the

immune system and a reduction in the circulation half-life.

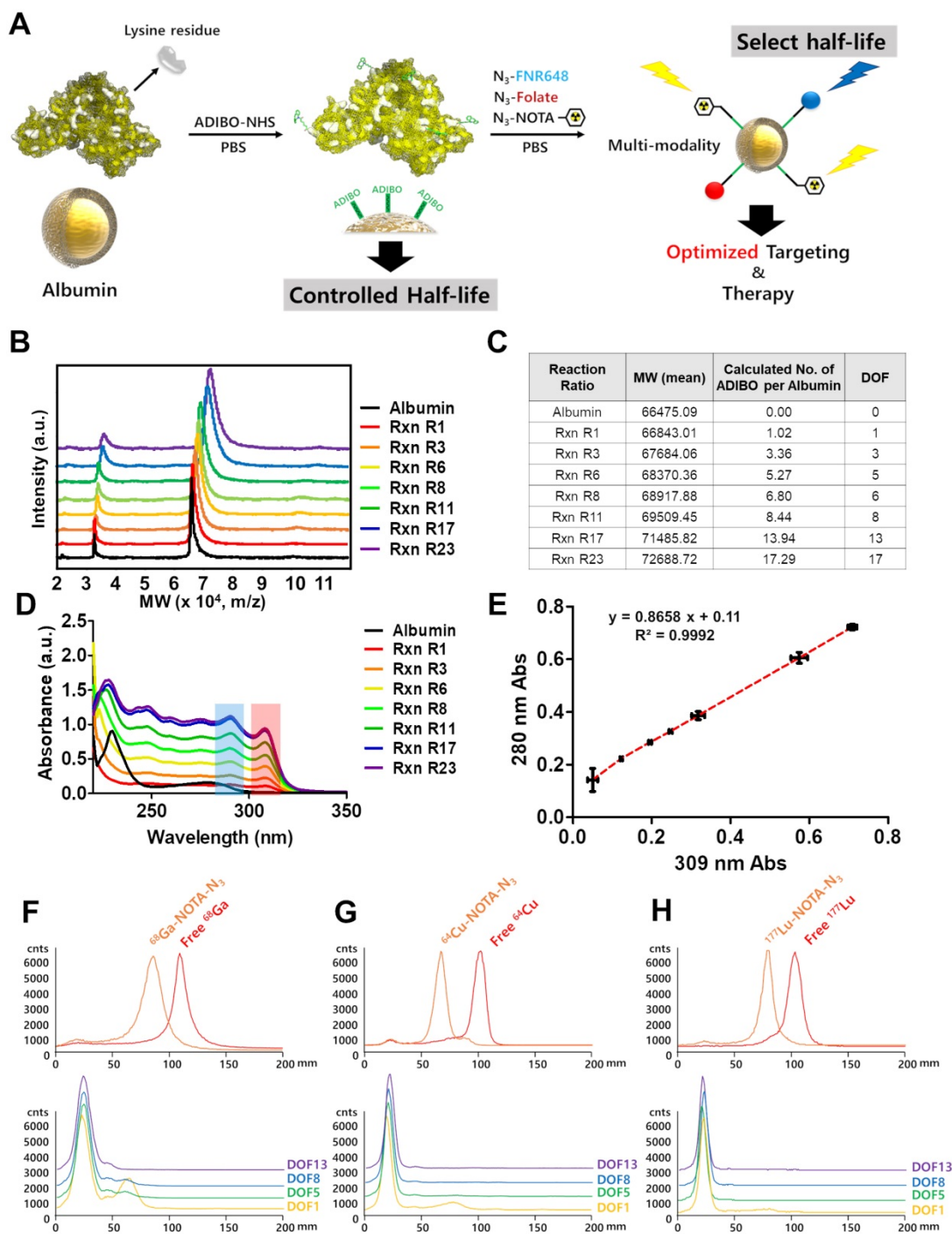


Figure 1. Synthesis and characterization of click chemistry-based albumin nanoplatform. (A) Schematic representation of click chemistry-based albumin nanoplatform. ADIBO-NHS: 2,5-dioxopyrrolidin-1-yl 4-azidobutanoate (N_3 -NHS), Azidobenzocyclooctyne-NHS ester, PBS: phosphate buffer solution, N_3 -NOTA: 2,2',2''-(2-(4-(3-(3-azidopropyl)thioureido)benzyl)-1,4,7-triazonane-1,4,7-triyl)triacetic acid, N_3 -FNR648: Flamma 648 azide. (B) Matrix-assisted laser desorption/ionization time of flight (MALDI-TOF) showed that mass increased according to the reaction ratio. (C) The increase in molecular weight according to reaction ratios and the number of attached ADIBO and DOF can be calculated. (D) UV-vis showed increased peak intensities at both a specific wavelength for albumin and ADIBO according to the reaction ratio. (E) The peak intensities of albumin and ADIBO correlated with a correlation coefficient (R^2) of 0.9992, indicating that an increased peak intensity at albumin wavelength is caused by the changed peak intensity of ADIBO. (F-H) Radio TLC chromatogram for confirmation of radiochemical yields of the three radioisotopes and click reaction efficiency of CANs with a radioisotope labeled N_3 -NOTA. The free radioisotope is shown in red, and the N_3 -NOTA labeled radioisotope in orange. ^{68}Ga labeling (F), ^{64}Cu labeling (G), and ^{177}Lu labeling chromatogram (H). Yellow, green, blue, and purple denote DOF1, DOF5, DOF8, and DOF13, respectively. Rxn R1, Rxn R3, Rxn R6, Rxn R8, Rxn R11, Rxn R17, Rxn R23: reaction molar ratio between ADIBO-NHS and albumin of 1.1:1, 3.4:1, 5.7:1, 8.1:1, 11.4:1, 17.2:1, 23:1, respectively.

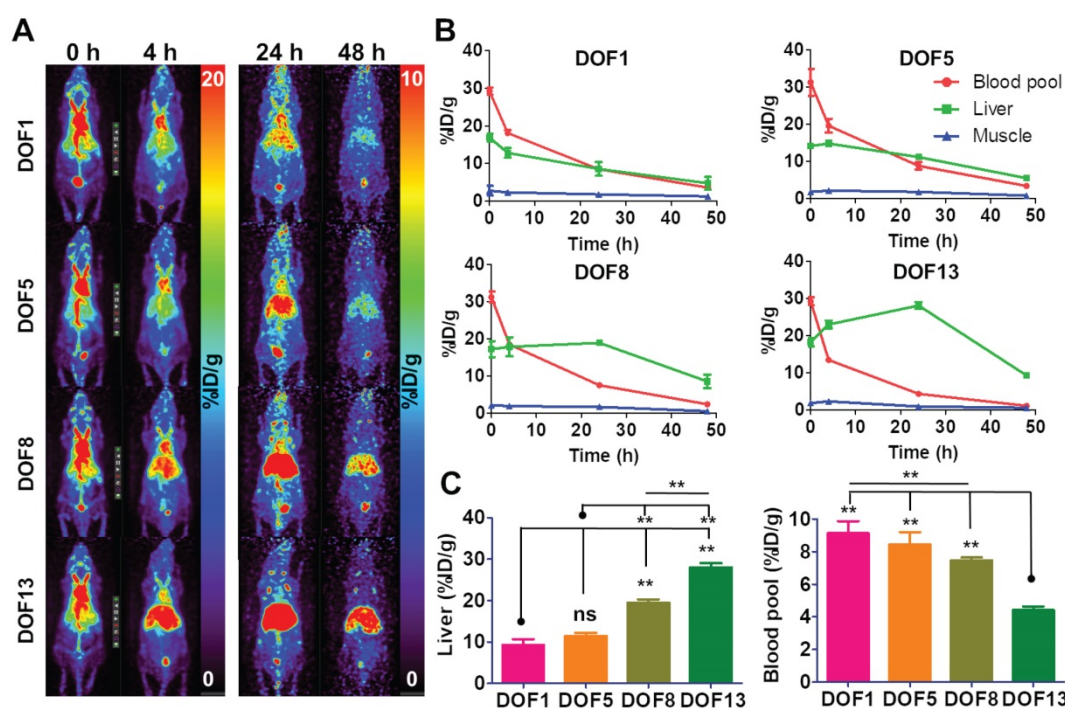


Figure 2. Alteration of biodistribution according to DOF. (A) Biodistributions of DOF1, DOF5, DOF8, and DOF13 were compared using serial *in vivo* PET imaging (n = 4 for each group). (B) The higher DOF groups showed faster clearance from the blood pool and higher uptakes in the liver than the lower DOF groups. (C) At 24 h after the injection, the DOF1 group showed lower liver uptake than the DOF8 and DOF13 groups. The DOF13 group showed lower liver uptake than the other three groups. However, there were no significant differences in blood pool and liver uptake between DOF1 and DOF5. DOF1: ^{64}Cu -CAN-DOF1 injected mouse group (n = 4); DOF5: ^{64}Cu -CAN-DOF5 injected mouse group (n = 4); DOF8: ^{64}Cu -CAN-DOF8 injected mouse group (n = 4); DOF13: ^{64}Cu -CAN-DOF13 injected mouse group (n = 4). **: P < 0.01.

Table 1. Table of *ex vivo* biodistribution of ^{64}Cu -CAN-FA (%ID/g) at 1, 4, 24, and 48 h post-injection in the KB tumor model

	1 h	4 h	24 h	48 h
Blood	22.80±1.84	12.57±0.71	2.86±0.42	1.01±0.37
Muscle	0.70±0.15	0.72±0.15	0.27±0.06	0.28±0.2
Heart	3.92±0.6	3.75±0.07	0.72±0.07	0.67±0.14
Lung	13.86±2.99	5.91±0.75	2.23±0.33	0.78±0.09
Liver	13.60±1.79	11.87±1.3	3.95±0.3	1.88±0.28
Spleen	4.60±0.41	2.90±0.36	0.78±0.06	0.66±0.08
Stomach	1.55±0.57	0.46±0.09	0.59±0.44	0.45±0.17
Intestine	5.24±0.59	6.57±1.28	2.78±0.35	0.65±0.22
Kidney	8.18±0.53	6.77±0.48	1.80±0.23	0.84±0.06
Bone	3.38±0.29	1.98±0.14	0.71±0.21	0.77±0.48
Tumor	3.56±0.33	5.17±0.51	5.81±0.55	5.49±0.91

In vitro folate receptor targeting ability of CAN-FA

After attaching folate and fluorescence dye to CAN using click chemistry reaction (CAN-FA-FI), we investigated the ability of the CAN to target the folate receptor *in vitro*. Firstly, we confirmed that the KB cells had a higher expression of the folate receptor than PC3 cells (Figure S6). The results of flow cytometry analysis revealed that CAN-FA-FI showed specific binding to KB cells, but not to PC3 cells (Figure 3A). In contrast, CAN-FI showed nonspecific binding to both cell lines. Furthermore, the radioactive saturation binding assay showed a high binding affinity ($K_d = 30$ nM) determined by nonlinear

regression (Figure 3B). The confocal microscopic image showed an intense fluorescence signal when CAN-FA-FI was treated with KB cells, whereas CAN-FI showed a small fluorescence signal under the same conditions. To further validate the specific uptake of CAN-FA-FI, KB cells were incubated with excess folic acid. The fluorescence signals were found to completely disappear, confirming the specific binding of CAN-FA-FI to folate receptors (Figure 3C).

In vivo targeting of ^{64}Cu -radiolabeled CAN-FA in folate receptor positive tumor

Serial *in vivo* positron emission tomography (PET) images were acquired at 10, 24, and 48 h after the intravenous injection of ^{64}Cu -CAN-FA (n=4) in KB

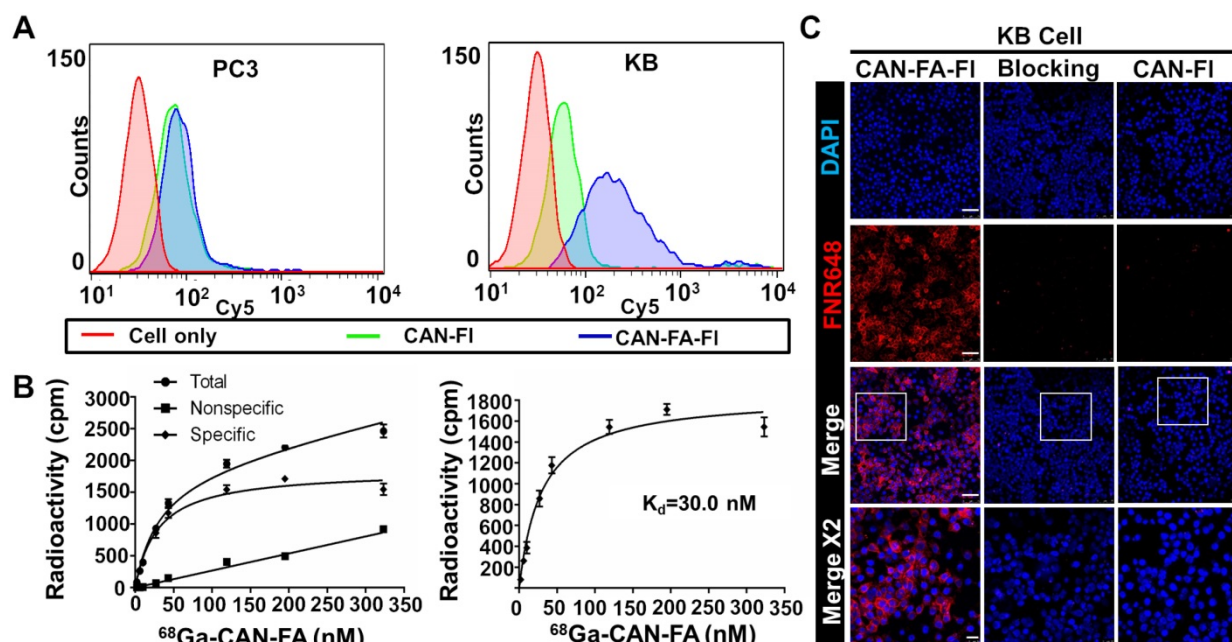


Figure 3. *In vitro* specific binding of folate targeting CAN. (A) Flow cytometry showed minimal nonspecific binding of CAN-FI in both PC3 and KB cells. CAN-FA-FI showed specific binding to KB but not PC3 cells. (B) The binding assay showed specific binding of ⁶⁸Ga-CAN-FA to KB cells with a binding affinity of 30 nM. (C) In confocal microscopy, CAN-FA-FI showed specific binding to KB cells while CAN-FI showed minimal nonspecific uptake. The excess folate showed complete blocking of CAN-FA-FI binding to KB cells. CAN-FI: fluorescence labeled CAN; CAN-FA-FI: folate and fluorescence-labeled CAN; DAPI: 4', 6-diamidino-2-phenylindole. Scale bar = 25 μ m (Merge \times 2) or 75 μ m (the others).

tumor-bearing xenograft via the tail vein. The PET images showed significant retention of activity in the blood and tumor (Figure 4A). The blood pool and liver uptake were 5.5 ± 0.2 , and 6.8 ± 0.6 percent of injected dose per gram (% ID/g) at 24 h, respectively. Moreover, substantial uptake was found in the tumor (7.6 ± 0.3 , 7.9 ± 0.5 , and 4.5 ± 0.2 %ID/g at 10 h, 24 h, and 48 h, respectively). The tumor uptake was higher than that of the blood pool and liver at 24 and 48 h after the injection (tumor to liver ratios = 0.9, 1.2, and 1.3 tumor to blood pool ratio = 0.9, 1.4, 2.1 at 10 h, 24 h, and 48 h post-injection, respectively) (Figure 4G).

In vivo imaging using ⁶⁴Cu-CAN demonstrates that there was no specific uptake in the KB tumor (Figure 4B) (n = 3). To confirm the specific accumulation of albumin radio-folate conjugate, ⁶⁴Cu-CAN-FA was co-injected with excess free folic acid (400 nmole / mouse) (n = 3). The tumor was significantly blocked (P < 0.01), confirming the specific uptake in tumors mediated by the folate receptor (Figure 4C). The quantified tumor uptake was significantly higher in the ⁶⁴Cu-CAN-FA injected group than the ⁶⁴Cu-CAN (P < 0.01) or ⁶⁴Cu-CAN-FA with blocking groups (P < 0.01) at all time points (Figure 4D). However, there was no significant difference in the uptake of the liver and blood pool between the groups at all time points (P = N.S) (Figure 4E, F). To determine the imaging probe effect of ⁶⁴Cu-CAN-FA, we performed an additional *in vivo* imaging study to examine the effect of methotrexate

on ⁶⁴Cu-CAN-FA. After injecting ⁶⁴Cu-CAN-FA with methotrexate, the PET images were acquired at 10 h, 24 h, and 48 h. The methotrexate injection was found to induce a significant decrease in tumor uptake. This suggested that the folate receptor in the tumor was blocked by injection of methotrexate; however, other organs showed a similar distribution of ⁶⁴Cu-CAN-FA (Figure S7).

An *ex vivo* biodistribution study of the ⁶⁴Cu-CAN-FA (n = 4) was performed in KB tumor-bearing mice at 1 h, 4 h, 24 h, and 48 h post-injection. ⁶⁴Cu-CAN-FA showed the highest uptake in the tumor (5.81 ± 0.55 % ID/g at 24 h and 5.49 ± 0.91 % ID/g 48 h p.i.), compared with the other organs (P < 0.01) (Figure 4H, I). Furthermore, an *ex vivo* biodistribution study of ⁶⁴Cu-CAN (n = 4) was carried out and compared with that of ⁶⁴Cu-CAN-FA. The tumor uptake was significantly higher in the ⁶⁴Cu-CAN-FA group compared to the ⁶⁴Cu-CAN group. The blood, lungs, liver, stomach, and kidneys showed significantly different uptakes between the groups (Figure S8).

Toxicity test of CAN to assess its biocompatibility

We performed the blood tests after the injection of CAN to determine if there was any deterioration of the kidney (Bun, Cr) or liver (AST, ALT) functions. Saline (as control), ⁶⁴Cu-CAN, or ⁶⁴Cu-CAN-FA was injected into the KB tumor-bearing mice. The BUN,

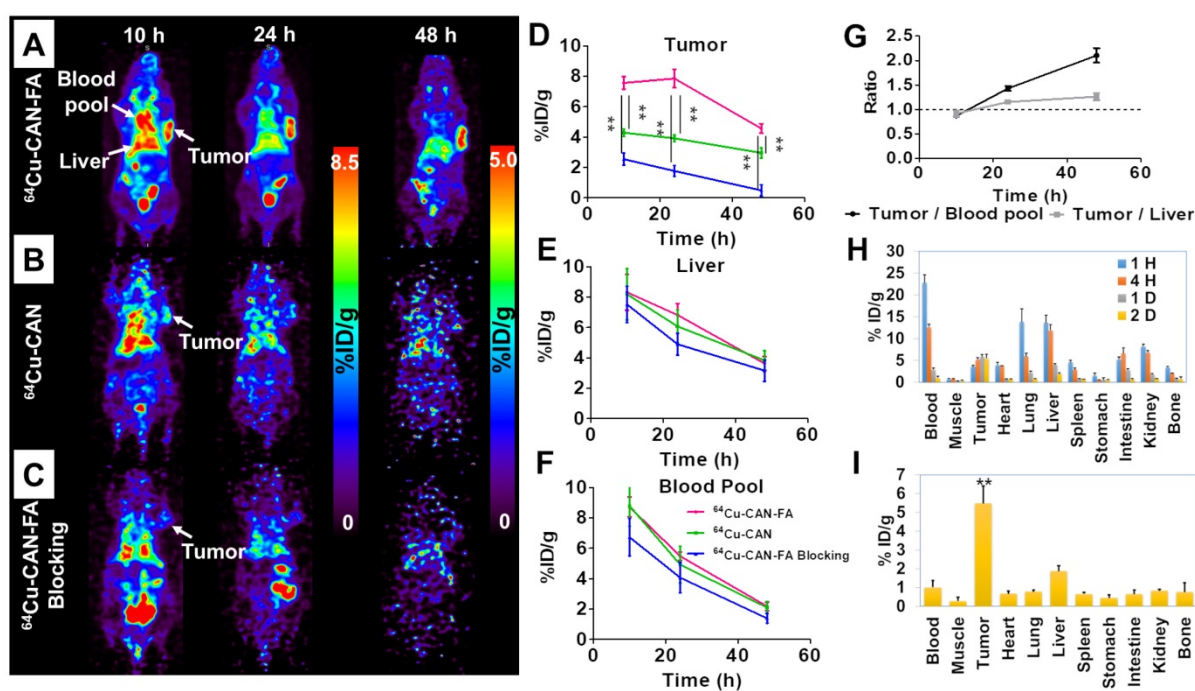


Figure 4. *In vivo* specific targeting of ^{64}Cu -CAN-FA. (A-C) In the KB tumor model, ^{64}Cu -CAN-FA showed substantial blood pool activity until 24 h after the injection. The tumor on the left shoulder showed a high uptake of the tracer. The tumor uptake was significantly lower in the ^{64}Cu -CAN and ^{64}Cu -CAN-FA blocking groups. (D-F) The quantified tumor uptake was significantly higher in the ^{64}Cu -CAN-FA group ($n = 4$) than the ^{64}Cu -CAN ($n = 3$) ($P < 0.01$) or ^{64}Cu -CAN-FA blocking groups ($n = 3$) ($P < 0.01$) at all time points (D). However, there was no significant difference in the uptake of the liver (E) and blood pool (F) between the groups at all time points ($P = \text{N.S.}$). (G) In ^{64}Cu -CAN-FA group, the tumor to blood pool ratio and tumor to liver ratio were higher than 1 at 24 and 48 h after the injection ($n = 4$). (H) *Ex vivo* biodistribution data at 1, 4, 24, and 48 h after the injection of ^{64}Cu -CAN-FA. ^{64}Cu -CAN: the KB cell tumor model group injected with ^{64}Cu -CAN; ^{64}Cu -CAN-FA: the KB cell tumor model group injected with ^{64}Cu -CAN-FA; ^{64}Cu -CAN-FA blocking: the KB cell tumor model group injected with ^{64}Cu -CAN-FA after injection of excess folate (400 nmole / mouse), **: $P < 0.01$.

creatinine, AST, and ALT were all within the normal range, indicating no acute toxic renal or hepatic effects *in vivo* (Figure S9, 10). Moreover, a morphological evaluation of the major organs was performed using H&E staining. The H&E stains indicated that there was no damage to the major organs, including the heart, lungs, liver, spleen, and kidneys (Figure S11). The hemolysis test was carried out to evaluate the blood compatibility. CANs with different DOFs showed no evidence of hemolysis effect (Figure S12). Finally, we performed the cell viability test after incubation of three cell lines (22RV1, MDA-MB231, and 293FT) with CAN up to 1 mg/mL using CCK-8 assay. There were no toxic effects of CAN in all 3 cell lines with over 95% cell viability (Figure S13). Taken together, our CAN showed no acute *in vivo* or *in vitro* toxicity.

Even with extensive research in the field of nanomedicine, the delivery efficiency of nanoparticles (NPs) is found to be generally low, with a median of 0.7% injected dose (%ID), as shown by pooled data analysis [39]. One of the main reasons for this low targeting efficiency is a short circulation half-life, which results from the fast elimination of NPs by the reticuloendothelial system (RES) [20]. In this regard, albumin is one of the most attractive nanoplateforms

because it is not immunogenic and circulates in the bloodstream for a long time without being eliminated by the RES. The most successful albumin-based drug carrier is Abraxane, a paclitaxel-albumin conjugate. Abraxane showed a favorable circulation half-life and clinical efficacies in the treatment of multiple types of advanced malignancies, including lung, pancreatic, and breast cancer [40, 41]. However, in many reported albumin nanoplateform studies, the circulation half-lives were short and varied widely. It is well known that the surface chemistry of NPs can determine the immune reaction and biodistribution [42]. Thus, altering the surface chemistry and size of albumin nanoplateforms through the addition of functional groups or loading drugs leads to immune reactions and subsequently the shortening of the circulation half-life.

Conventionally, $^{99\text{m}}\text{Tc}$ -labeled HSA ($^{99\text{m}}\text{Tc}$ -HSA) has been used in nuclear medicine field for blood pool imaging, however, it has a very short circulation half-life (32 minutes) (Figure S14) [14]. For the $^{99\text{m}}\text{Tc}$ labeling of HSA, an excessive amount of reducing agent was used to cleave disulfide bonds in albumin. Similarly, in one study, indocyanine green (ICG) dye was conjugated after disulfide bond cleavage of HSA (HSA-ICG), and the HSA-ICG showed a limited

circulation half-life (2.8 h) with a high liver uptake [43]. However, recent labeling methods without using reducing agent showed a longer circulation half-life (4.8 h) [16, 17]. Therefore, using a reducing agent to albumin may alter the surface chemistry of albumin and cause an immune response that decreases the circulation time. Two similar studies were reported that conjugated the dyes to albumin using hydrophobic interaction [44] [45]. Although the circulation half-lives had not been reported, one study showed a high tumor uptake with a low liver uptake [44], while the other showed a high liver and low tumor uptake, indicating the RES clearance of the nanoplatform [45]. One potential reason for this difference is that the latter study used dialysis solution with a pH of 10 to remove the unbound dye. The size of the albumin nanoplatform seems to affect the circulation time less. For example, Abraxane has a size of 130–150 nm and a long circulation-time. Furthermore, a 100-nm sized ¹³¹I-labeled albumin-paclitaxel nanoparticles showed a very long circulation half-life (31.9 h). The neutral conjugation method may be attributed to the long circulation half-life [46]. To summarize, harsh conditions such as low or high pH or the addition of reducing agents may result in a short circulation half-life in albumin nanoplatforms, while the size of the nanoplatforms seems to be less affected by the immune response. In our study, we performed click-chemistry reactions in mild aqueous condition for functionalization, and thus, were able to obtain a long circulation half-life and a high tumor targeting efficiency.

Changes in the DOF were also found to significantly alter the biodistribution of the albumin nanoplatform, which emphasizes the importance of a precise control of the nanoplatform parameters. Our click chemistry-based albumin nanoplatform can precisely control the DOF and number of functional groups. Furthermore, we developed the method to calculate the DOF using simple UV-vis after validation with MALDI TOF. Furthermore, our CAN can be easily produced at larger scales. There was a minimal batch to the batch difference regarding size, charge, number of conjugated ADIBO moieties, and *in vivo* biodistribution. Albumin solution (5 mg/mL) was used for the reaction on a 60-mL scale. After the reactions, the final albumin concentration was 1.85 mg/mL in 130 mL, and the total yield was confirmed to be 80%. Finally, the animal images showed no difference before and after the scale-up (Figure S15).

The limitation of this study is that the therapeutic effect of the nanoplatform was not tested, although the CAN was successfully labeled with a therapeutic radioisotope, ¹⁷⁷Lu. The theranostic ability of our CAN is under investigation. Moreover, the

DOF value of five in our CANs may be a small number for drug loading or further functionalization. If there is a need for further functionalization, increasing the DOF may be an option, with the corresponding sacrifice of circulation half-life. However, based on facile multi-functionalization of CAN, we believe that the CAN may be utilized for a wide range of specialized theranostic agents.

Conclusions

We developed CAN with precisely controllable DOF and long circulation half-life. The CAN was easily functionalized for *in vivo* imaging and specific tumor targeting. As such, it may therefore be an ideal strategy for biomedical applications, with precisely controlled DOF, favorable biodistribution, and facile functionalization. Furthermore, the ability to alter its biodistribution according to the DOF will be beneficial for the development of other types of successful albumin-based nanoplatforms.

Supplementary Material

Supplementary figures and tables.

<http://www.thno.org/v09p3398s1.pdf>

Acknowledgments

We would like to thank the Korea Institute of Radiological & Medical Sciences for providing radioisotopes. Hyung-Jun Im was supported by National Research Foundation of Korea (NRF) (NRF-2017R1D1A1B03035556, and NRF-2019M2D2A1A01058210), and Ministry of Health and Welfare Korea (HI18C0886). Yun-Sang Lee was supported by Radiation Technology R&D program (NRF-2017M2A2A7A01021401) through the National Research Foundation of Korea (NRF). Keon Wook Kang was supported by Radiation Technology R&D program (NRF-2017M2A2A7A01070923) through the National Research Foundation of Korea (NRF). Jung Young Kim as supported by a Nuclear Research and Development Program of the National Research Foundation of Korea (NRF) grant funded by the Korean government (NRF-2017M2A2A6A02019904).

Competing Interests

The authors have declared that no competing interest exists.

References

1. Carter DC, He XM, Munson SH, Twigg PD, Gernert KM, Broom MB, et al. Three-dimensional structure of human serum albumin. *Science*. 1989; 244: 1195-8.
2. Karimi M, Bahrami S, Ravari SB, Zangabad PS, Mirshekari H, Bozorgomid M, et al. Albumin nanostructures as advanced drug delivery systems. *Expert Opin Drug Deliv*. 2016; 13: 1609-23.
3. Liu Z, Chen X. Simple bioconjugate chemistry serves great clinical advances: albumin as a versatile platform for diagnosis and precision therapy. *Chem Soc Rev*. 2016; 45: 1432-56.

4. Yousefpour P, Chilkoti A. Co-opting biology to deliver drugs. *Biotechnol Bioeng.* 2014; 111: 1699-716.
5. Sudlow G, Birkett DJ, Wade DN. The characterization of two specific drug binding sites on human serum albumin. *Mol Pharmacol.* 1975; 11: 824-32.
6. Kragh-Hansen U. Evidence for a large and flexible region of human serum albumin possessing high affinity binding sites for salicylate, warfarin, and other ligands. *Mol Pharmacol.* 1988; 34: 160-71.
7. Trynda-Lemiesz L. Paclitaxel-HSA interaction. Binding sites on HSA molecule. *Bioorg Med Chem.* 2004; 12: 3269-75.
8. Watanabe N, Shirakami Y, Tomiyoshi K, Oriuchi N, Hirano T, Higuchi T, et al. Direct labeling of macroaggregated albumin with indium-111-chloride using acetate buffer. *J Nucl Med.* 1997; 38: 1590-2.
9. Hunt AP, Frier M, Johnson RA, Berezenko S, Perkins AC. Preparation of Tc-99m-macroaggregated albumin from recombinant human albumin for lung perfusion imaging. *Eur J Pharm Biopharm.* 2006; 62: 26-31.
10. Zhao S, Wang W, Huang Y, Fu Y, Cheng Y. Paclitaxel loaded human serum albumin nanoparticles stabilized with intermolecular disulfide bonds. *MedChemComm.* 2014; 5: 1658-63.
11. Geng T, Zhao X, Ma M, Zhu G, Yin L. Resveratrol-Loaded Albumin Nanoparticles with Prolonged Blood Circulation and Improved Biocompatibility for Highly Effective Targeted Pancreatic Tumor Therapy. *Nanoscale Res Lett.* 2017; 12: 437-.
12. Gao F, Cai P, Yang W, Xue J, Gao L, Liu R, et al. Ultrasmall [64Cu]Cu Nanoclusters for Targeting Orthotopic Lung Tumors Using Accurate Positron Emission Tomography Imaging. *ACS Nano.* 2015; 9: 4976-86.
13. Chiu N-T, Lee B-F, Hwang S-J, Chang J-M, Liu G-C, Yu H-S. Protein-losing Enteropathy: Diagnosis with 99mTc-labeled Human Serum Albumin Scintigraphy. *Radiology.* 2001; 219: 86-90.
14. Wang YF, Chuang MH, Chiu JS, Cham TM, Chung MI. On-site preparation of technetium-99m labeled human serum albumin for clinical application. *Tohoku J Exp Med.* 2007; 211: 379-85.
15. Suzuki C, Higaki S, Nishiaki M, Mitani N, Yanai H, Tada M, et al. 99mTc-HSA-D scintigraphy in the diagnosis of protein-losing gastroenteropathy due to secondary amyloidosis. *J Gastroenterol.* 1997; 32: 78-82.
16. Basuli F, Li C, Xu B, Williams M, Wong K, Coble VL, et al. Synthesis of fluorine-18 radio-labeled serum albumins for PET blood pool imaging. *Nucl Med Biol.* 2015; 42: 219-25.
17. Jain A, Pandey U, Gamre N, Sarma HD, Dash A. Development of 68Ga labeled human serum albumin for blood pool imaging: a comparison between two ligands. *J Radioanal Nucl Chem.* 2017; 313: 661-8.
18. Steinhäuser IM, Langer K, Strebhardt KM, Spänkuch B. Effect of trastuzumab-modified antisense oligonucleotide-loaded human serum albumin nanoparticles prepared by heat denaturation. *Biomaterials.* 2008; 29: 4022-8.
19. Lee SP, Im HJ, Kang S, Chung SJ, Cho YS, Kang H, et al. Noninvasive Imaging of Myocardial Inflammation in Myocarditis using (68)Ga-tagged Mannosylated Human Serum Albumin Positron Emission Tomography. *Theranostics.* 2017; 7: 413-24.
20. Im H-J. Excretion and Clearance. In: Lee DS, editor. *Radionanomedicine: Combined Nuclear and Nanomedicine.* Cham: Springer International Publishing; 2018: 347-68.
21. Kolb HC, Finn MG, Sharpless KB. Click Chemistry: Diverse Chemical Function from a Few Good Reactions. *Angew Chem Int Ed Engl.* 2001; 40: 2004-21.
22. Li N, Binder WH. Click-chemistry for nanoparticle-modification. *J Mater Chem.* 2011; 21: 16717-34.
23. Yi G, Son J, Yoo J, Park C, Koo H. Application of click chemistry in nanoparticle modification and its targeted delivery. *Biomaterials Research.* 2018; 22: 13.
24. Huang T, Hu P, Banizs AB, He J. Initial evaluation of Cu-64 labeled PARPi-DOTA PET imaging in mice with mesothelioma. *Bioorg Med Chem Lett.* 2017; 27: 3472-6.
25. Ma W, Fu F, Zhu J, Huang R, Zhu Y, Liu Z, et al. 64Cu-Labeled multifunctional dendrimers for targeted tumor PET imaging. *Nanoscale.* 2018; 10: 6113-24.
26. Ke C-Y, Mathias CJ, Green MA. Folate-receptor-targeted radionuclide imaging agents. *Adv Drug Deliv Rev.* 2004; 56: 1143-60.
27. Lodhi NA, Park JY, Hong MK, Kim YJ, Lee Y-S, Cheon GJ, et al. Development of 99mTc-labeled trivalent isonitrile radiotracer for folate receptor imaging. *Bioorg Med Chem.* 2019.
28. Lu Y, Low PS. Folate-mediated delivery of macromolecular anticancer therapeutic agents. *Adv Drug Deliv Rev.* 2012; 64: 342-52.
29. Hilgenbrink AR, Low PS. Folate Receptor-Mediated Drug Targeting: From Therapeutics to Diagnostics. *J Pharm Sci.* 2005; 94: 2135-46.
30. Bettio A, Honer M, Müller C, Brühlmeier M, Müller U, Schibli R, et al. Synthesis and Preclinical Evaluation of a Folic Acid Derivative Labeled with 18F for PET Imaging of Folate Receptor-Positive Tumors. *J Nucl Med.* 2006; 47: 1153-60.
31. Muller C, Forrer F, Schibli R, Krenning EP, de Jong M. SPECT study of folate receptor-positive malignant and normal tissues in mice using a novel 99mTc-radiofolate. *J Nucl Med.* 2008; 49: 310-7.
32. Xu C, Shi S, Feng L, Chen F, Graves SA, Ehlerding EB, et al. Long Circulating Reduced Graphene Oxide-Iron Oxide Nanoparticles for Efficient Tumor Targeting and Multimodality Imaging. *Nanoscale.* 2016; 8: 12683-92.
33. Swinehart DF. The Beer-Lambert Law. *J Chem Educ.* 1962; 39: 333.
34. Hernandez R, Aluicio-Sarduy E, Grudzinski J, Pinchuk A, Engle J, Weichert J. Choice of radiometal influences the tumor targeting and biodistribution properties of theranostic alkylphosphocholine chelates in vivo. *J Nucl Med.* 2018; 59: 533.
35. Wang B, He X, Zhang Z, Zhao Y, Feng W. Metabolism of nanomaterials in vivo: blood circulation and organ clearance. *Acc Chem Res.* 2013; 46: 761-9.
36. Zhu M, Nie G, Meng H, Xia T, Nel A, Zhao Y. Physicochemical properties determine nanomaterial cellular uptake, transport, and fate. *Acc Chem Res.* 2013; 46: 622-31.
37. Al-Jamal KT, Nunes A, Methven L, Ali-Boucetta H, Li S, Toma FM, et al. Degree of Chemical Functionalization of Carbon Nanotubes Determines Tissue Distribution and Excretion Profile. *Angew Chem.* 2012; 51: 6389-93.
38. Roser M, Fischer D, Kissel T. Surface-modified biodegradable albumin nano- and microspheres. II: effect of surface charges on in vitro phagocytosis and biodistribution in rats. *Eur J Pharm Biopharm.* 1998; 46: 255-63.
39. Wilhelm S, Tavares AJ, Dai Q, Ohta S, Audet J, Dvorak HF, et al. Analysis of nanoparticle delivery to tumours. *Nat Rev Mater.* 2016; 1: 16014.
40. Ma P, Mumper RJ. Paclitaxel Nano-Delivery Systems: A Comprehensive Review. *J Nanosci Nanotechnol.* 2013; 4: 1000164.
41. Miele E, Spinelli GP, Miele E, Tomao F, Tomao S. Albumin-bound formulation of paclitaxel (Abraxane®) ABI-007) in the treatment of breast cancer. *Int J Nanomed.* 2009; 4: 99-105.
42. Lee DS, Im HJ, Lee YS. Radionanomedicine: widened perspectives of molecular theragnosis. *Nanomedicine.* 2015; 11: 795-810.
43. Sheng Z, Hu D, Zheng M, Zhao P, Liu H, Gao D, et al. Smart Human Serum Albumin-Indocyanine Green Nanoparticles Generated by Programmed Assembly for Dual-Modal Imaging-Guided Cancer Synergistic Phototherapy. *ACS Nano.* 2014; 8: 12310-22.
44. Chen Q, Wang C, Zhan Z, He W, Cheng Z, Li Y, et al. Near-infrared dye bound albumin with separated imaging and therapy wavelength channels for imaging-guided photothermal therapy. *Biomaterials.* 2014; 35: 8206-14.
45. Gao F-P, Lin Y-X, Li L-L, Liu Y, Mayerhöffer U, Spent P, et al. Supramolecular adducts of squaraine and protein for noninvasive tumor imaging and photothermal therapy in vivo. *Biomaterials.* 2014; 35: 1004-14.
46. Tian L, Chen Q, Yi X, Wang G, Chen J, Ning P, et al. Radionuclide I-131 Labeled Albumin-Paclitaxel Nanoparticles for Synergistic Combined Chemo-radioisotope Therapy of Cancer. *Theranostics.* 2017; 7: 614-23.